Materials Chemistry and Physics 260 (2021) 124094

Contents lists available at ScienceDirect

Materials Chemistry and Physics

journal homepage: www.elsevier.com/locate/matchemphys

Synthesis of metal-free nitrogen-enriched porous carbon and its electrochemical sensing behavior for the highly sensitive detection of dopamine: Both experimental and theoretical investigation

Palanisamy Rupa Kasturi [a], Trichy Kuppusamy Aparna [b], Agnes Lincy Arokiyanathan [c], Senthilkumar Lakshmipathi [c,***], Ramanathan Sivasubramanian [b,**], Yun Sung Lee [d,****], Ramakrishnan Kalai Selvan [a,*]

[a] Energy Storage and Conversion Devices Laboratory, Department of Physics, Bharathiar University, Coimbatore, 641046, Tamil Nadu, India
[b] Electrochemical Sensor and Energy Materials Laboratory, Department of Chemistry, PSG Institute of Advanced Studies, Coimbatore, Tamil Nadu, 641 004, India
[c] Atomistic Simulation Laboratory, Department of Physics, Bharathiar University, Coimbatore, 641046, Tamil Nadu, India
[d] Faculty of Applied Chemical Engineering, Chonnam National University, Gwangju, 500-757, South Korea

HIGHLIGHTS

- The nitrogen-inherited foam-like porous carbon is sequestered from the starch of Artocarpus *heterophyllus* seeds.
- It exhibits a turbostratic structure, high degree of graphitization, with porous architecture for dopamine sensing.
- It showed good catalytic activity with a low limit of detection (2.74 nM), and superior sensitivity (4.64 μA μM $^{-1}$cm $^{-2}$).
- The first-principle calculations used to determine the molecular-level interaction between the porous carbon and dopamine.
- The interaction between dopamine and the nitrogen-enriched carbon sheet was stronger than the oxygen-rich sheet.

GRAPHICAL ABSTRACT

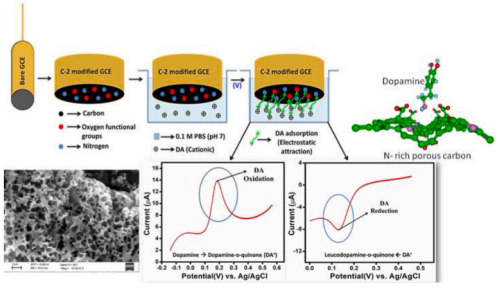

ARTICLE INFO

Keywords:
Artocarpus heterophyllus seed
Porous carbon
Electrochemical sensor
Dopamine
The computational study

ABSTRACT

In this study, a nitrogen-inherited foam-like porous carbon was sequestered from the starch of Artocarpus *heterophyllus* seeds. The obtained carbon material was used as a sustainable electrode for the electrochemical detection of dopamine biomolecule. The material exhibited a turbostratic structure, high degree of graphitization, strong carbon-nitrogen bonding, high surface area, and porous architecture. It showed good catalytic activity with a low onset potential (80 mV), wide linear responses (30–90 μM and 200–400 μM), a low limit of

* Corresponding authors.
** Corresponding author.
*** Corresponding authors.
**** Corresponding author.
E-mail addresses: lsenthilkumar@buc.edu.in (S. Lakshmipathi), rss@psgias.ac.in (R. Sivasubramanian), leeys@chonnam.ac.kr (Y.S. Lee), selvankram@buc.edu.in (R.K. Selvan).

https://doi.org/10.1016/j.matchemphys.2020.124094
Received 19 June 2020; Received in revised form 4 September 2020; Accepted 23 November 2020
Available online 25 November 2020

detection (2.74 nM), and superior sensitivity (4.64 μA μM $^{-1}$cm $^{-2}$). The results indicated that the porous architecture and organic functionalities on the surface provided fast electron transfer at the electrode/electrolyte interface. Moreover, it offered superior stability, reproducibility, and biocompatibility toward dopamine sensing in real samples. Furthermore, first-principle calculations were performed in both the gas and aqueous phase to determine the molecular-level interaction between the porous carbon and dopamine. The results indicated that the interaction between dopamine and the nitrogen-enriched carbon sheet was stronger (−0.64 eV) than the oxygen-rich sheet. The atoms-in-molecules analysis, charge density difference analysis, and Fukui function plots indicated a charge transfer from the biomolecules to the carbon sheet. Overall, the theoretical findings confirmed the observed experimental results.

1. Introduction

Dopamine (DA) sensing is an essential research element in the field of neuroscience. In general, DA [4-(2-aminoethyl) benzene-1,2-diol] belongs to the catecholamine and phenylethylamine (PEA) family, functioning as a neurotransmitter in the brain. Neurotransmitters are chemical messengers (amine functional groups) situated throughout the brain through which neurons carry nerve impulses as messages from one nerve cell to another through receptors. Some of the chief neurotransmitters present in the brain are glutamate, gamma-aminobutyric acid, serotonin, dopamine, and norepinephrine. Among these, DA (a catecholamine neurotransmitter) is spread throughout the body (hypothalamus, olfactory bulb, midbrain substantia nigra and ventral tegmental area, periaqueductal gray, and retina), and performs various functional activities such as cognition, metabolism, cardiovascular regulation, and renal and hormonal balance. This catecholamine biomolecule [$C_6H_3(OH)_2$-CH_2-CH_2-NH_2] is also known as a "motivation molecule," a "sympathomimetic drug," and a "reward and pleasure chemical" as it is responsible for thoughts, feelings (pleasure and pressure), emotional disturbances (stress and poor motivation), reinforcement, and behavioral changes in human beings [1]. Therefore, DA is crucial for transmitting signals from the body to the brain. However, an insufficient amount of DA secretion in synaptic clefts may induce neurological disorders/illness, including schizophrenia, depression, psychosis (hallucinations), autism, obsessive-compulsive disorder, and Parkinson's disease [2,3]. Excess stimulation of dopamine with pleasure drugs (cocaine, nicotine, and heroin) causes victims to become addicted to drugs eventually.

Therefore, it is imperative to adopt a method that is highly efficient for the sensitive and selective detection of dopamine [4–7]. Electrochemical sensing has attracted much attention owing to its low cost, easy detection, and faster response time. DA is an electroactive molecule that can be detected easily at room temperature and without the use of any enzymes or redox additives. However, its detection is hindered owing to interference from other biomolecules, such as glucose, L-ascorbic acid (AA), and uric acid (UA). Therefore, it is crucial to develop a sensor material to recognize DA with high sensitivity and high selectively.

Nanomaterials based on metals [6], metal oxides [7], mixed metal oxides [8], hydroxides [9], sulfides [10], and heteroatom-doped/decorated carbonaceous materials including porous carbon [11], activated carbon [12], carbon nanotubes (CNTs) [13], graphene [14], and reduced graphene oxide (rGO) [15]were used as sensing elements for the electrochemical detection of DA. Among these nanomaterials, metal/metal oxide-free carbon-based materials are excellent candidates owing to their low cost, tunable surface chemical properties, and easy availability. These characteristics, together with the strong adsorption quality of carbon toward organic species, lead to an enhanced electrochemical response. However, the fast electron transfer, impressive surface-to-volume ratio, greater number of active sites, high degree of porosity, presence of negatively charged surface functionalities, and good reactivity and stability make biomass-derived porous carbon an attractive electrode compared with other electrode materials [16]. The built-in heteroatoms (N, B, S, and P) and functional groups

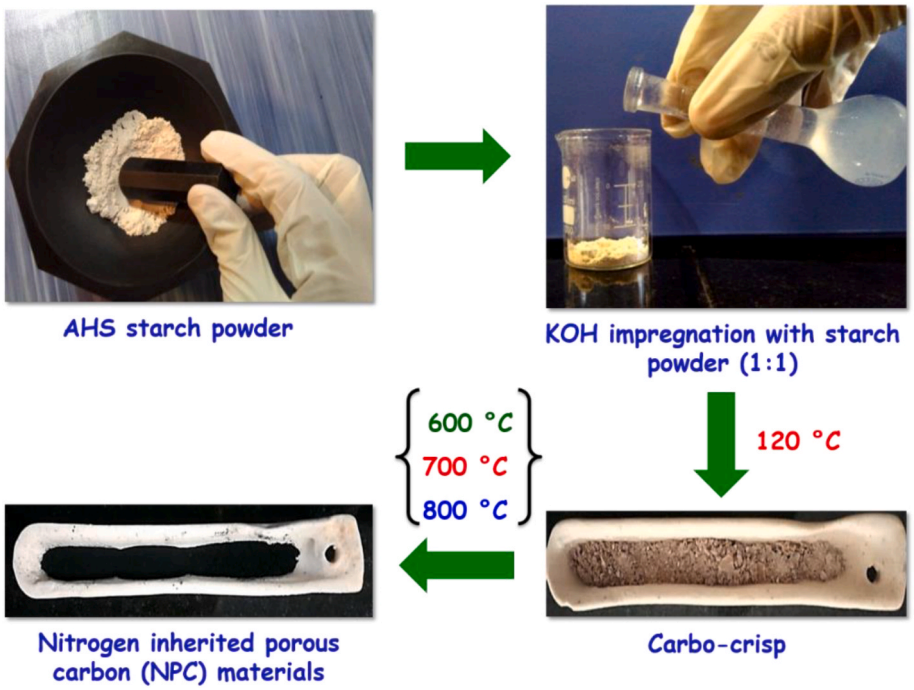

Scheme 1. Preparation of activated carbon from AHS starch powder.

(–OH, –COOH) on active carbon make it more reactive and feasible toward the analyte during sensing [11,12]. Porous carbon materials sequestered from various biomass precursors have been successfully used for the sensitive electrochemical detection of DA. Recently, kiwi skin-derived carbon delivered a detection limit of 0.16 μM, with a linear response of 2–2000 μM toward DA detection [17]. Porous carbon derived from natural silk cocoons (79 nM with 0.6–140 μM) [18], commercial activated carbon (50 μM with 50–1000 μM) [19], sucrose [20], pumpkin skin-derived carbon (0.06 μM, with 1–65 μM) [21], tal palm leaves (0.078 μM, with 5–200 μM) [22], and pork liver (10.6 nmol L^{-1} with 0.5–280 μmol L^{-1}) [23] has also been reported.

In the present work, *Artocarpus heterophyllus* seed starch was used as a precursor to prepare nitrogen-inherited porous carbon materials by using a temperature-controlled carbonization method. The *Artocarpus heterophyllus* tree is an evergreen renewable energy source that contains surplus amounts of electroactive components such as sucrose, phenolic additives, and heteroatom functionalities, increasing its usefulness in the field of electrochemistry [24–26]. The obtained nitrogen-inherited porous carbon materials had high surface areas, porosities, and organic functionalities. Interestingly, a nitrogen-inherited porous carbon (NPC)-modified glassy carbon electrode (GCE) achieved a low onset potential, wide linear response, and a low limit of detection (LOD) toward DA detection with higher selectivity and sensitivity. Density functional theory (DFT) calculations were also performed to gain a molecular-level understanding of the interaction between the NPC and the biomolecules of dopamine and uric acid. The results obtained will further improve electrode materials for the sensing of biomolecules.

2. Experimental methods and materials

2.1. Chemicals and solutions

Potassium hydroxide pellets (KOH), ethanol (C_2H_5OH), L-AA ($C_6H_8O_6$), and UA ($C_5H_4N_4O_3$) were purchased from Himedia. Dopamine hydrochloride ($C_8H_{12}ClNO_2$) was bought commercially from Sigma-Aldrich and used without further purification. A phosphate buffer solution (PBS) at pH 7.0 was prepared by using 0.1 M K_2HPO_4 and KH_2PO_4 solutions.

2.2. Preparation of nitrogen-inherited porous carbon materials

The *Artocarpus heterophyllus* seeds starch (AHS) powder was dried in the oven at 100 °C for 12 h [24,25]. For the chemical activation, 1 g of AHS powder was mixed with 0.5 g of KOH and stirred overnight. The obtained activated carbon precursor was crushed well and carbonized in a tubular furnace at various temperatures (600, 700 and 800 °C) for 1 h under constant nitrogen flow at a heating rate of 10 °C/min. Then, the sequestered carbon samples were collected and washed with double distilled (D-D) water, ethanol, and 0.5 M HCl until achieving pH 7. Then, the samples were dried at 80 °C for 24 h to remove moisture, crushed to a fine powder, and sealed in an airtight container. The prepared NPC materials are denoted as NPC-1 (600 °C), NPC-2 (700 °C), and NPC-3 (800 °C). The experimental procedure is represented in Scheme 1.

2.3. Characterization

X-ray diffraction (XRD) patterns were recorded on a PAN analytical XRD system using CuKα radiation (λ = 1.54 Å). Fourier transform infrared spectroscopy (FTIR) measurements were performed using a JASCO FT/IR-6600 instrument. Morphological analysis was carried out using high magnification with field emission scanning electron microscopy (FE-SEM) on a Carl Zeiss Microscopy Ltd., UK & SIGMA instrument at 20 kV operating voltage. Raman spectra were obtained using a Raman dispersive spectrometer (Lab Ram HR 800, Horiba, Japan). X-ray photoelectron spectroscopy (XPS) was carried out using a Thermo Scientific Multi-lab 2000 system. The surface area, pore size, and pore distribution of the samples were determined using nitrogen adsorption/desorption at 77 K using a Micrometrics ASAP 2010 surface area analyzer the Brunauer–Emmett–Teller (BET) method, and the Barrett–Joyner–Halenda (BJH) method, respectively. The electrochemical behavior of activated carbon was recorded using cyclic voltammetry (CV) and differential pulse voltammetry (DPV) using a Biologic VSP-150 instrument, a multichannel VSP potentiostat/galvanostat (France), and an electrochemical workstation with EC-Lab® software package.

2.4. Fabrication of electrodes for electrochemical biosensor

To fabricate the electrodes, a mixed solution containing the activated carbon sample powder (NPC; 85 wt%), D-D water, isopropyl alcohol, and Nafion (5 wt%) were sonicated for 15 min to obtain a thick black slurry. Then, 5 μL of the obtained black slurry was mixed with 1 mL of isopropyl alcohol and sonicated for another 30 min. At the same time, the surface of a GCE (3 mm diameter) was thoroughly cleaned using alumina powder (3.0 μm), ethanol, and D-D water and sonicated for 10 min. From the obtained solution, 10 μL of the solution was drop cast onto the GCE and kept untouched for 30 min to obtain an NPC-modified GCE (NPC-GCE). For sensing applications, the NPC-GCE, Ag/AgCl (3 M KCl), and platinum wire were used as the working, reference, and counter electrodes, respectively. PBS (5 mL) was used as the supporting electrolyte, and all the electrochemical measurements were carried out at room temperature. In a PBS solution (0.1 mol L^{-1}, pH 7.0, containing 10 mmol L^{-1} of DA, and UA), the DPV and CV measurements were conducted from −0.2 to 0.6 V, with a pulse amplitude and pulse width of 100 mV s^{-1} and 50 ms, respectively. The lowest concentration of the analyte was determined by the LOD using the following equation [11]:

$$LOD = \frac{3S_D}{m} \quad (1)$$

where, 3 is the confidence level parameter (statistical confidence 99%), S_D is the standard deviation from the blank measurement, and m is the slope from the calibration graph (S/N = 3).

2.5. Real sample analysis

DA and UA analytes usually exist in the human system in the form of blood serum and urine, respectively. The serum sample (50 μL) was added to 5 mL of 0.1 M PBS, and the electrochemical DPV technique was employed in the potential region of 0.1–0.5 V vs. Ag/AgCl at a scan rate of 100 mV s^{-1}. In the buffer solution, different concentrations of DA and UA were injected into the serum and urine samples during the electrochemical measurements and the percent recoveries (%) were estimated from the respective linear regression plots (Equation (2)).

$$\%\ R = \frac{F_c}{I_c} \times 100 \quad (2)$$

where, % R is the percentage recovery, F_c is the final concentration of the analyte, and I_c is the initial concentration of the analyte.

2.6. Computational details

All the theoretical calculations were performed using DFT calculations within the generalized gradient approximation (GGA) of the Perdew–Burke–Ernzerhof (PBE) approach as implemented in the Vienna Ab-initio Simulation Package (VASP) [27–32]. The electronic wave functions were expanded on a plane-wave basis set using a kinetic energy cut-off of 450 eV. The geometries were optimized until the energy was lower than 1×10^{-4} eV and the force on each atom was less than 0.01 eV/Å. The Brillouin zone was sampled using a Monkhorst–Pack k-mesh and a grid of 4 × 4 × 1 was chosen for the geometrical optimization, whereas a denser grid of 8 × 8 × 1 was used for the electronic properties calculations [33]. Dispersion corrections were included using

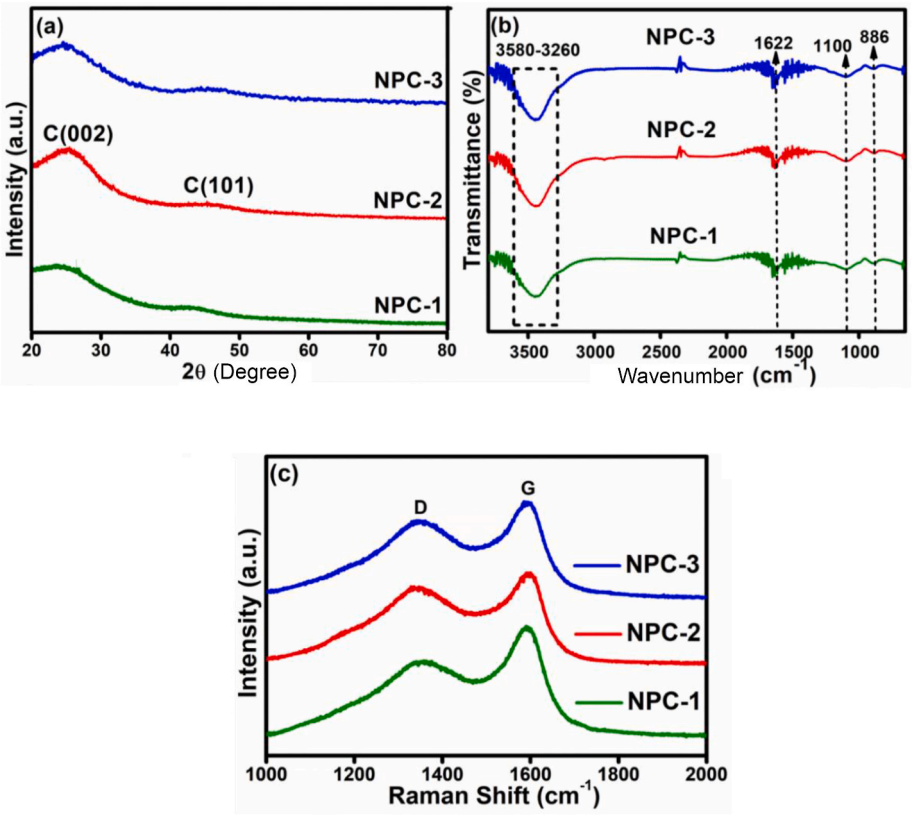

Fig. 1. a) XRD pattern, b) FTIR spectra, and c) Raman spectra of NPC materials.

Grimme's empirical (DFT-D3BJ) method [34,35]. The optimized gas-phase structures were subjected to the implicit solvent interaction with water as the solvent (because the pH of the electrolyte was 7 PBS) using VASP sol [36]. The adsorption energy (E_{ads}) of biomolecules (DA/UA) on the NPC sheet is given by the equation

$$E_{ads} = E_{complex} - (E_{AC} + E_{biomolecule})\ eV \quad (3)$$

where $E_{complex}$, E_{AC}, and $E_{biomolecule}$ are the total energies of the NPC sheet interacting with a biomolecule, an isolated NPC sheet, and an isolated biomolecule, respectively.

3. Results and discussion

3.1. Physicochemical properties of nitrogen-inherited porous carbon

Fig. 1a shows the XRD patterns of the KOH-treated nitrogen-inherited porous carbon (NPC) materials. It exhibits two broad peaks at 20–30° and 44.5°, which are ascribed to the (002) and (101) plane reflections of the amorphous carbon matrix, respectively. The occurrence of the (002) broad peak is due to the creation of a microporous network because of KOH activation, whereas the XRD peak corresponding to the (101) plane indicates the degree of graphitization among the carbon atoms. The low intensities of the peaks suggest the highly disordered graphitic nature of the NPC materials [7–9]. The chemical functionalities on the surfaces of the NPC materials were qualitatively assessed through FTIR analysis (Fig. 1b). The clearly noticeable broadband (3580-3260 cm^{-1}) indicated O–H or N–H stretching vibration modes owing to the hydroxyl groups present in the polysaccharides [7]. The band observed at ~1622 cm^{-1} is due to the presence of an aromatic ring (C=C). The 1100 cm^{-1} band is due to C–O–C in the carboxyl, alcohol, phenolic esters, and ketonic conjugated structures [10–12]. The 886 cm^{-1} band in the spectra reveals the aromatic C–H (out-of-plane bending) functionalities existing on the surfaces of the NPC materials. The –OH bonding is due to the KOH activation, and the carboxylic functional groups are due to polymeric components present in the biomass precursor [13–18]. The presence of organic functionalities enables the carbon surface to adsorb positively charged DA ions with electrostatic interaction and accelerate electron transfer during the electrochemical reaction [7,19].

The graphitization degree of the activated carbon samples is easily understood from the I_D/I_G ratio in the Raman spectra (Fig. 1c), where I_G is the intensity of the G-band at ~1597 cm^{-1} and I_D is the intensity of the D-band at ~1350 cm^{-1} belongs to sp^2 and sp^3 hybridization of carbon atoms with the hexagonal graphitic ring, defects, and disorders [15,19]. The XRD peaks evidenced at 2θ peaks of 20–30° and 44.5° corresponding to the (002) and (101) planes are ascribed to the D-band and G-band, respectively [37]. Moreover, the I_D/I_G ratios calculated for NPC-1, NPC-2, and NPC-3, wherein the order of 0.95, 0.87, and 0.97, respectively. It is seen that the I_D/I_G ratio is less for NPC-2 (0.87) compared to NPC-3 (0.97). It signifies the presence of less number of defects and increase in graphitization degree with increase in temperature [20–22]. On the other hand, the NPC-3 loses its stability at 800 °C wherein the heterocyclic C-N bond breaks leading to structural deformation. The details are given in the subsequent sections. Hence it is believed that the performance of NPC-2 will be high when compared to NPC-3.

The specific surface areas of the NPC materials were acquired from BET analysis (Fig. 2a). All the carbon samples exhibited type-IV adsorption/desorption isotherms, as shown by the hysteresis curve at high relative pressures. Hence, the AHS-derived NPC materials prepared from KOH activation at various carbonization temperatures were microporous materials that collectively exhibited mesoporous volumes [20]. The specific surface areas and porous network parameters of the NPC materials are given in Table 1. NPC-2 carbonized at 700 °C under N_2 atmosphere exhibited a large surface area (756 $m^2\ g^{-1}$) and large micropore volume (0.59 $cm^3\ g^{-1}$) in accordance with the BET (Fig. 2a)

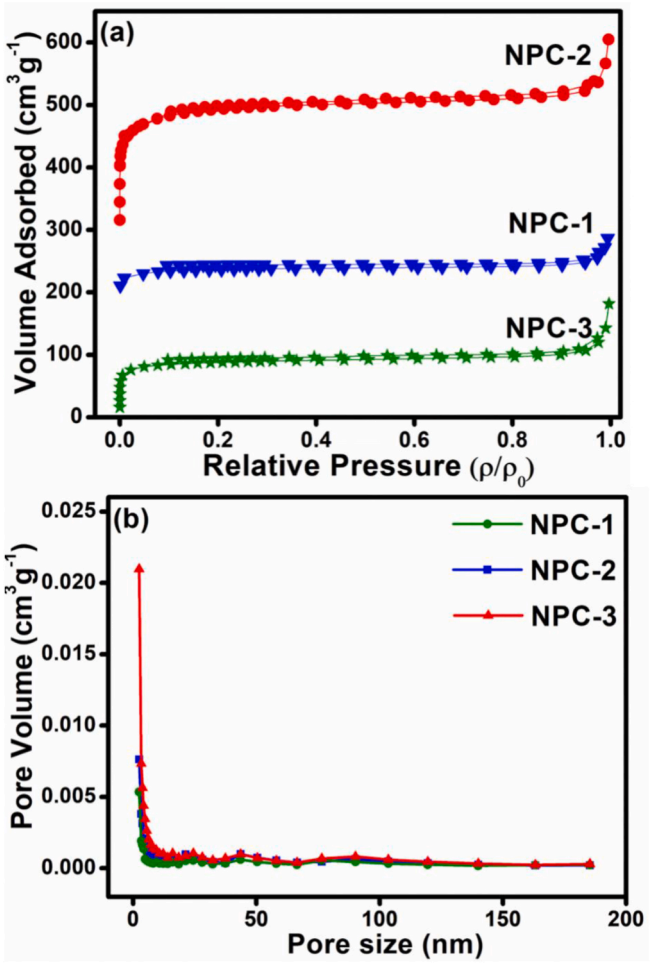

Fig. 2. a) N_2 adsorption/desorption isotherms and b) BJH pore-size distribution curve of NPC materials.

Table 1
Calculated parameters from BET and XPS analysis.

NPC materials	S_{BET} (m^2 g^{-1})[a]	V_{total} (cm^3 g^{-1})[b]	D (nm)[c]	Composition (atom % from XPS)		
				C	N	O
NPC-1	383.3	0.22	2.6	83.9	0.89	15.14
NPC-2	756.5	0.59	2.2	85.14	6.18	8.68
NPC-3	173.05	0.13	3.0	85	1.45	13.55

[a] Specific surface area.
[b] Total pore volume.
[c] Mean pore diameter.

and BJH (Fig. 2b) analyses. This high surface area provided a large number of active sites for the organization of organic functional groups and nucleation sites for ion adsorption during the electrochemical reaction. At high temperature (800 °C), extreme burn-off broke the defined carbon pore network which leads to reduction in structural stability. Therefore, the surface area and the porosity are abruptly decreased (Table 1) as evident by the SEM images of NPC-3 in the succeeding sections. Intuitively, the large surface area and extensive porosity of NPC-2 was expected to provide high ionic conductivity, facilitate fast electron transportation, and substantially improve the electrochemical sensitivity of the system toward DA detection [23–26].

The elemental composition of NPC materials was analyzed using XPS (Fig. 3 and Fig. S1). The XPS survey spectra (Fig. 3a) indicated the presence of C1s, N1s, and O1s elements on the activated carbon materials, and their respective elemental compositions are presented in Table 1. A high percentage of C and N was found in the NPC-2 sample owing to the influence of temperature, which was optimum for KOH molecules to create active sites and anchor a large amount of nitrogen and oxygen functionalities on the NPC surface. The amount of nitrogen on the carbon surfaces decreased in the order of NPC-2 > NPC-3 > NPC-1, with the increased oxygen content showing the same order. This indicates that an excess amount of oxygen prevented the addition of nitrogen functionalities on the surface of the carbon with respect to temperature [13,16,20]. Therefore, carbonization at 700 °C not only increased the surface area and porosity, but it also resulted in a higher amount of nitrogen content on the surface of the NPC-2 as compared to NPC-1 and NPC-3. Therefore, from the XPS analysis, 700 °C was found to be the optimum carbonization temperature to sequester carbon materials from AHS with a high yield percentage of carbon and nitrogen elements.

The high-resolution deconvoluted spectrum of C1s (Fig. 3b) revealed the graphitic carbon peaks of NPC-2 corresponding to C–C (284.1 eV), C–O–C (285.9 eV), and O–C=O (288.3 eV), indicating the high percentage of carbon species in the sample [9,33]. The O1s peaks (Fig. 3c) at 531.8, 532.0, 533.8 eV are assigned to C–OH, C–C=O, and C=O, respectively, indicating the organization of oxygen atoms inherited owing to the burning of organic matter present in the AHS [25]. The high-resolution N1s spectra of the NPC materials exhibited two types of C–N bonds: pyridinic-N (398.3 eV) and pyrrolic-N (400.2 eV). The existence of nitrogen species in the NPC materials strongly depends on the carbonization temperature. For NPC-1 prepared at 600 °C, the majority of C–N bonds exhibited a pyrrolic structure (Fig. S1), and the highest content of N species was 0.89 at. wt%. With the increase in carbonization temperature (700 °C), the N1s deconvoluted spectrum (Fig. 3d) of NPC-2 exhibited two peaks, pyrrolic-N (400.2 eV) and pyridinic-N (398.3 eV), with a rapid increase in N species to 6.18 at. wt%. The inherited nitrogen species are owing to the heterocyclic rings formed during carbonization, which are condensed into aromatic structures of carbon with strong C–N bonding under inert atmosphere [39]. These nitrogen functionalities are expected to provide good wettability and biocompatibility for the porous carbon network during chemisorption. Moreover, the N species participate in fast electron transportation (graphitic-N) and induce more active sites (pyridinic- N) for the adsorption of DA during electrochemical detection [12,15,17]. On the other hand, the N1s spectrum of NPC-3 was found to have two peaks, pyrrolic-N (400.8 eV) and pyridinic-N (398.3 eV), but the amount of N content was reduced to 1.45 at. wt% owing to the low thermal stability of pyrrolic-N [38]. This high pyrolysis conditions lead to breaking of the heterocyclic C-N bonds, thereby the N evolves as gases.

Fig. 4 shows the scanning electron microscopic images of the NPC materials. The smooth, flake-like structure (Fig. 4a) with no porosity represents the inability of KOH to penetrate the surface of the carbon matrix at 600 °C. Fig. 4b shows interconnected foam-like cylindrical pores with sharp edges on the surface of the activated carbon (NPC-2) material. It indicates that KOH had completely corroded the char network and constructed porosity when the temperature reached 700 °C, resulting in a highly porous carbon network with a large surface area of 756 m^2 g^{-1} (BET analysis) [40–42]. At 700 °C, the KOH molecules ultimately eroded the matrix of carbon and formed a porous network along their pathway. On the other hand, the presence of more number of aggregated structure without any porous morphology was observed in the SEM images of NPC-3 sample (Fig. 4c) due to the high carbonization temperature. This leads to structural deformation and low surface area and decreased total pore volume. The transmission electron microscopy (TEM) image (Fig. 4d) substantiates the well-defined edges with foam-like mesoporous channels of NPC-2.

The actual phenomena behind the KOH activation of *Artocarpus heterophyllus* seed starch are that during carbonization, the KOH molecules are transformed into K_2O and water molecules through a dehydration reaction (Equation (4)). The carbon products are disbursed and

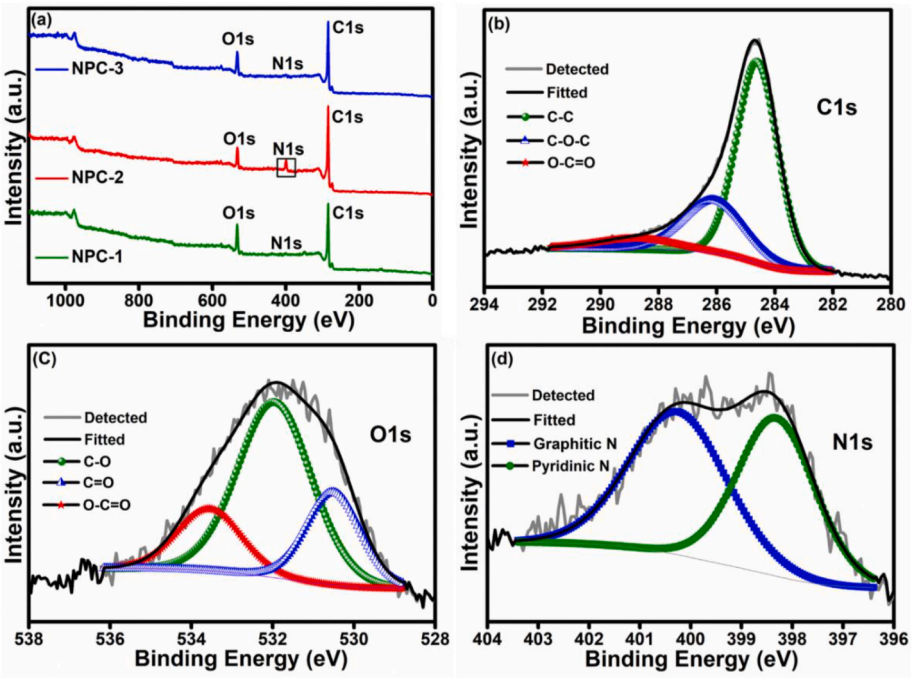

Fig. 3. a) XPS survey spectra of NPC materials and the deconvoluted spectrum of b) C 1s, c) O 1s, and d) N 1s of NPC-2 material.

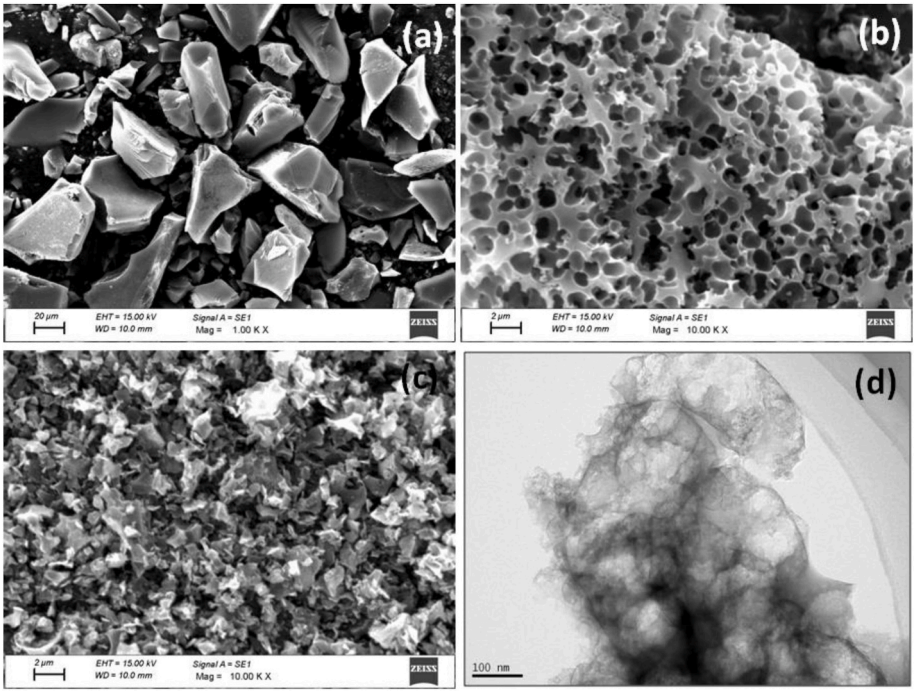

Fig. 4. FE-SEM images of a) NPC-1, b) NPC-2, and c) NPC-3 and d) the TEM image of NPC-2.

emitted as CO_2 and H_2 (Equations (5) and (6)). The reaction between K_2O and CO_2then leads to the formation of K_2CO_3 (Equation (7)) [18,19,22].

$$2KOH \rightarrow K_2O + H_2O \quad (4)$$

$$C + H_2O \rightarrow CO + H_2 \quad (5)$$

$$CO + H_2O \rightarrow CO_2 + H_2 \quad (6)$$

$$CO_2 + K_2O \rightarrow K_2CO_3 \quad (7)$$

Electrochemical impedance spectroscopy (EIS) analysis was carried out to establish the conductive nature of bare GCE and the representative NPC-2 carbon-modified GCE (Fig. 5) in 0.1 M PBS and a 5 mM $K_4[Fe(CN)_6]$ solution in the frequency range between 10 kHz and 1 Hz at a fixed potential of 0.2 V*vs.* Ag/AgCl. For both electrodes, a semicircle (ion migration) was found in the high-frequency region and linearity (ions have enough time to migrate was attained in the high-frequency region [23]. The attained Nyquist plot was fitted with an equivalent circuit, shown in the inset of Fig. 5, and the corresponding parameters are provided in Table 2 [23–26]. The R_s, R_{ct}, and W values were less for the

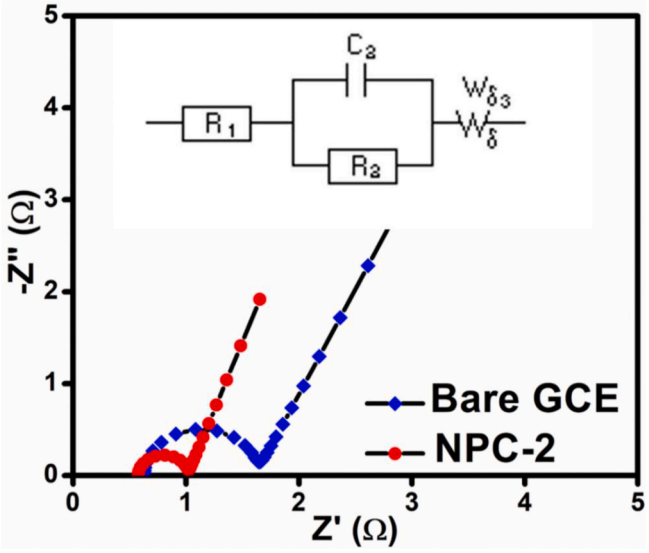

Fig. 5. Nyquist plot of bare GCE and NPC-2 in 0.1 M PBS and 5 mM $K_4[Fe(CN)_6]$ in the frequency range between 10 kHz and 1 Hz.

Table 2
Parameters obtained from Nyquist plot for bare GCE and NPC-2–modified GCE.

Electrode	R_s (Ω)	R_{ct} (Ω)	C_{dl} (MF)	W	A_{real} (cm^2)	σ
Bare GCE	0.68	0.788	23.7	0.7842	1.885	26.9
NPC-2–modified GCE	0.51	0.2871	68.6	0.3115	3.43	49

NPC-2-modified GCE compared to bare the GCE owing to the high surface-to-volume ratio and the porous architecture of the carbon surface. Collectively, these parameters largely influence the electrochemical performance. R_s is a measure of the mobility of ions through the pores and the electrical resistivity of the electrode, R_{ct} is responsible for the change in IR drop and sensitivity, and W prevents electrolyte diffusion into the electrode architecture [39–41]. Moreover, the active surface area (A_{real}) and roughness factor (σ) were 3.43 cm^2 and 49, respectively, for the NPC-2 modified GCE. Overall, component each estimated from the Nyquist plot had a significant effect on the properties of NPC-2 modified GCE (Table 2).

3.2. Non-enzymatic electrochemical properties for dopamine sensor

Fig. 6a shows the CV curves of NPC-GCE in the presence of DA (100 μM) in 0.1 M PBS electrolyte (pH 7) at a scan rate of 100 mV s^{-1} toward the response of DA oxidation. Among the prepared NPC-GCEs (Fig. 6a), the GCE modified with NPC-2 provided a high oxidation peak (185 mV) of DA at a very low onset potential of 80 mV compared to NPC-1 (130 mV) and NPC-3 (120 mV) [10,13], as well as the DA oxidation current obtained in the order of NPC-2 (13.95 μA) >NPC-1 (8.7 μA) > NPC-3 (4.8 μA). The high performance of NPC-2 towards DA oxidation is attributed to the high nitrogen content, which further enhances the conductivity of the modified electrode. Besides, the high surface area of NPC-2 compound provides more active sites for the ion adsorption to takes place. Fig. 6b shows the CV curves of the GCE modified with the NPC-2 electrode in the same electrolyte measured at scan rates of 100–1000 mV s^{-1}. With increasing scan rate, the peak current gradually increases, with a slight shift in the oxidation and reduction peaks in the positive and negative directions, respectively [6,42–44]. Therefore, a strong DA oxidation peak with a high current with respect to scan rate is observed in the CV curves. The reduction peak also observed (Fig. 6b) corresponding with the oxidation peak owing to the rebounding DA molecules, and the decrease in current is due to the blockage of voids on the electrode surface area [45]. This observation indicates that the NPC-2 modified GCE exhibited a fast electron transfer process with high current with increasing scan rate. Both the oxidation (I_{oxi}) and reduction (I_{red}) peak currents increase with scan rates of 100–1000 mV s^{-1}, offering linear regression values (R^2) of 0.98931 and 0.97176, respectively (Fig. 6b inset). The linearity indicates that oxidation is a diffusion-controlled phenomenon.

Fig. S2a shows the CV curves of NPC-2 modified GCE electrode in 0.1 M PBS electrolyte with different concentrations of DA (100–700 μM) measured at 100 mV s^{-1}. With increasing the DA concentration, the observed positive peak shift with high current indicates the feasibility of NPC-2 as the sensor element toward DA detection. As shown in Fig. S2b, the oxidation (I_{oxi}) peak current increases with increasing DA concentration, offering a linear regression value (R^2) of 0.9778. The highest peak current of NPC-2 modified GCE indicates the essential importance of high nitrogen functionalities built into the electrode surface, which anchors catalytic sites for the DA molecules, thus facilitating electron transport through the PBS for enhanced electrochemical activity [12]. Similarly, the reduction of DA observed as a high and sharp cathodic peak at 135 mV (Scheme 2). The presence of nitrogen functionalities (6.8 at wt%) and optimum oxygen functional groups promote electron acceleration, whereas the higher surface area and porosity of the NPC-2 modified GCE offer good conductivity for enhanced electrochemical determination of DA at a very low onset potential [26,37,38].

The DPV technique was also adapted to determine the DA detection on the NPC-2 modified GCE electrode due to its high resolution and sensitivity as compared to other electrochemical techniques (Fig. 7). A gradual increase in current observed in the DPV response of the NPC-2

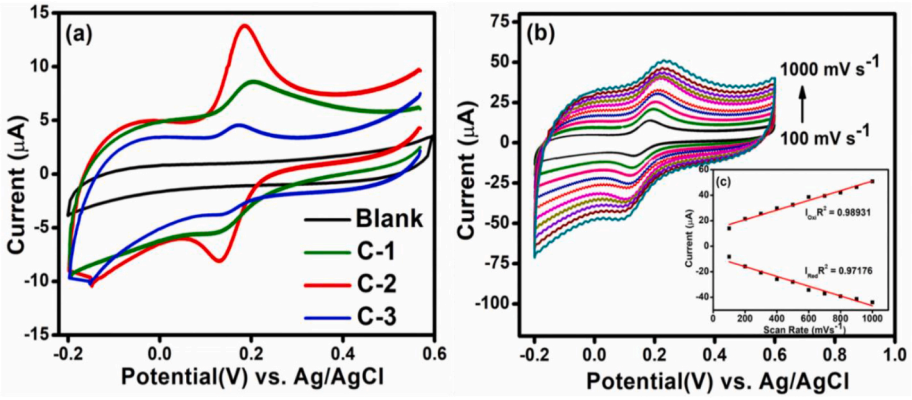

Fig. 6. a) CV profiles of NPC-GCE electrodes in 0.1 M PBS with DA at 100 mV s^{-1} and b) CV profiles of NPC-2 sensor recorded at scan rates of 100–1000 mV s^{-1}. Inset:Corresponding linear regression calibration plot of peak oxidation and reduction scan rates*vs.* current.

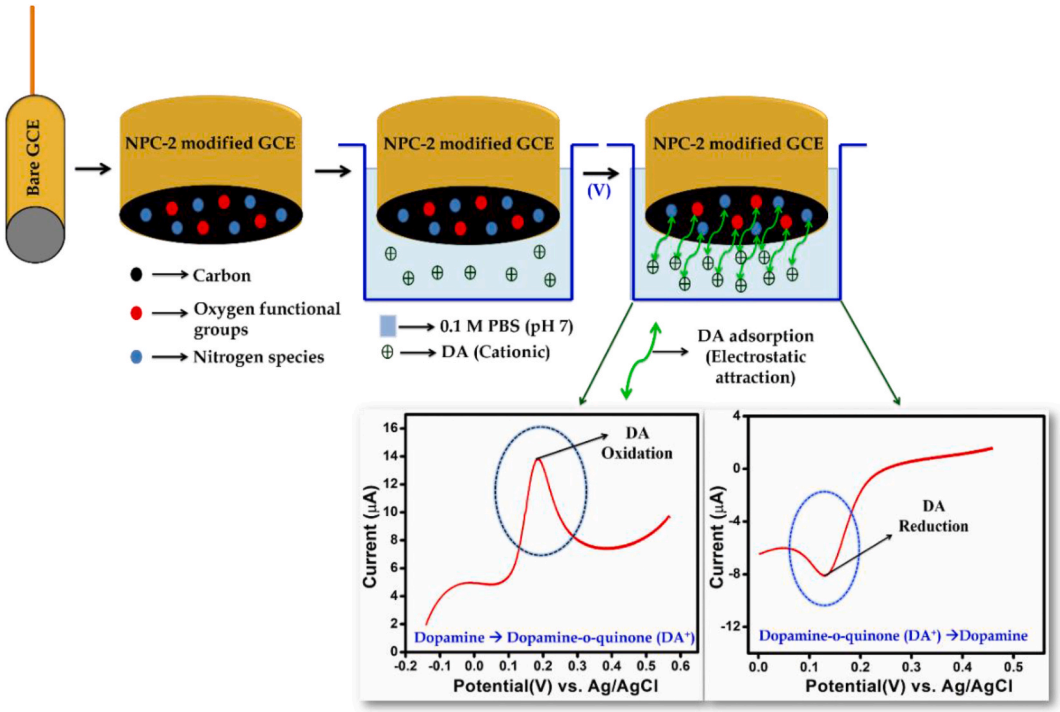

Scheme 2. Electrochemical detection mechanism of DA by NPC-2–modified GCE.

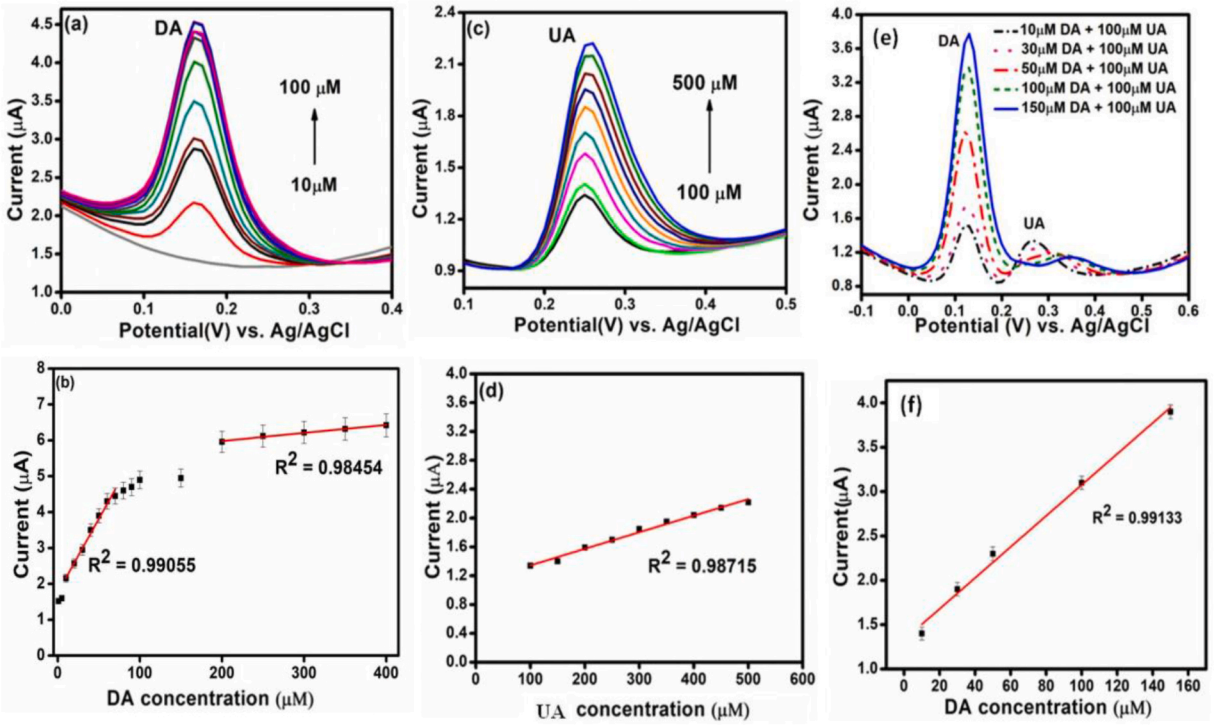

Fig. 7. a) DPV responses of NPC-2 in 0.1 M PBS containing different concentrations of dopamine, (b) the corresponding linear regression calibration plot of different concentrations of DA (μM) *vs.* current (μA), c) DPV responses of NPC-2 in 0.1 M PBS containing different concentrations of uric acid, and d) the corresponding linear regression calibration plot of different concentration of UA (μM) *vs.* current (μA). e) DPV response for the selective detection of DA in the presence of UA (100 μM), and f) linear regression calibration plot of different concentrations of DA (μM) *vs.* current (μA).

modified GCE at increasing concentrations of DA (10–100 μM) in 0.1 M PBS (Fig. 7a). Such an increase in current (2.17–4.5 μA) with every 10 μM increase in DA concentration is due to the strong electrostatic attraction between the chemical functionalities situated on the carbon surface holding an electronegative charge and the electropositive charge of DA biomolecules during oxidation [10,41–44]. Accordingly, in response to the DA concentration and anodic peak current, two different linear regression plots obtained (Fig. 7b). The initial plot ranging from 30 to 90 μM, corresponds to the low concentration of DA, with a linear regression value (R^2) of 0.99055. The second plot ranging from 200 to

Table 3
Comparison of various carbon-based sensors for the electrochemical detection of DA.

Sample No.	Sensor	LOD	Linear Range (DA)	Ref.
1	Silk	79 nM	0.6–140 μM	[18]
2	Activated carbon (Commercial)	50 μM	50–1000 μM	[19]
3	Sucrose	–	4×10^{-5}– 1×10^{-3} M	[20]
4	Kiwi skin	0.16 μM	2–2000 μM	[17]
5	Pumpkin skin	0.06 μM	1–65 μM	[21]
6	Tal palm leaves	0.078 μM	1–100 μM	[22]
7	Pork liver	10.6 nM L^{-1}	0.5–280 μM	[23]
8	AHS starch	2.74 nM	30–90 μM 200–400 μM	Present work

400 μM, has a linear regression value (R^2) of 0.98454. Therefore, these ranges are assigned as the linear DA detection response ranges of NPC-2 modified GCE in 0.1 M PBS (pH 7). It is seen that two different linear ranges are found from the calibration graph. At low concentration the diffusion followed by adsorption of ions on the electrode surface will be less and the response current increases linearly. However as the concentration is increased more adsorption of ions occurs leading to more accumulation of ions near the interface. As a result there will be a deviation in the peak potential at high concentration which further results in the break in linear ranges in the calibration graph [11]. The linear regression equation ($y = 0.0325x + 0.00264$) gives a low LOD (2.74 nM) toward DA (Table 3). Moreover, the sensitivity of the NPC-2 was obtained from the ratio between the slope (0.000297 μA mM^{-1}) and the surface area of the GCE (0.07 cm^2), and therefore the sensitivity was found to be 4.64 μA μM^{-1} cm^{-2}. In a recent study, Ahammad et al. achieved a sensitivity of about 2.693 μA μM^{-1} cm^{-2} with porous tal palm carbon nanosheets for the determination of DA [22]. Fig. 7c shows the DPV curves of the NPC-2–modified GCE for the oxidation of UA at different concentrations. The oxidation occurred at 250 mV vs. Ag/AgCl and the corresponding linear regression plot ($y = 0.0023x + 1.1143$) gave the linear detection range of 100–500 μM and a detection limit of 38 nM for UA (Fig. 7d).

The selectivity of the NPC-2 modified GCE toward DA was deduced from the DPV curves (Fig. 7e). Fig. 7e shows the DPV curves for different concentrations of DA while keeping the concentration of UA constant (100 μM) in 0.1 M PBS solution. The difference in the peak separation obtained from the DPV profile is large enough to detect DA without the interference of UA. The exact reasoning for the high selectivity of the NPC-2 modified GCE sensor is because of the π–π interaction between the carbon basal edges and the DA phenyl rings [39,43,44]. This interaction provides maximum electroactive sites for the adsorption of DA species on the electrode surface and selectively separates DA from UA [11,13]. The corresponding linear regression plot ($y = (4.5 \times 10^{-4})x + 1.732$) is displayed with it R^2 value (0.9945) (Fig. 7f). These findings infer that NPC-2 possesses good selectivity to sense DA in the presence of UA.

3.3. Analysis of human serum and urine samples for practical applications

The practical applicability of the NPC-2-modified GCE in real-time examples was investigated by adding known quantities of DA and UA in 0.1 M PBS containing human serum and urine samples. 50 μM serum/urine samples were diluted in PBS solution, and different concentrations of DA and UA (50, 100, and 150 μM) were added. The percentage of recovery was evaluated, and the results are given in Table 4. These values indicate that the NPC-2 modified GCE is a promising sensor for the detection of DA and UA in real samples. The interference effect of biomolecules such as urea and glucose and ions such as KCl and KNO_3 during DA detection on the NPC-2 modified GCE was studied, and the results were plotted as a bar diagram (Fig. S3a). The addition of biomolecules had only a slight influence on the oxidation peak current of DA with respect to concentration. The nitrogen species anchored on NPC-2 significantly influenced the selectivity of various analytes that participated with DA molecules [46]. This finding suggests that the detection of DA by the NPC-2 modified GCE is highly sensitive as it is free from the common interfering compounds.

Table 4
Real sample analysis and the calculated parameters of NPC-2–modified GCE.

Real Sample	Quantity Added (μM)		Estimated Quantity (μM)			
	DA	UA	DA	% R	UA	% R
Serum	50	50	49.81	99.62	49.93	99.86
	100	100	98.97	98.97	99.91	99.91
	150	150	149.56	99.70	149.26	99.50
Urine	50	50	49.75	99.50	49.87	99.74
	100	100	99.92	99.92	98.97	98.97
	150	150	149.85	99.90	149.91	99.94

The NPC-2 modified GCE was tested to evaluate its reproducibility and stability toward DA detection. To determine the reproducibility, 10 mM DA was added to 0.1 M PBS solution, and the corresponding oxidation peak current was measured for the initial and 100th cycle at a scan rate of 100 mVs^{-1} (Fig. S3b). A 7.14% deviation in the current value was observed, which indicates that the electrochemical response of the NPC-2 modified GCE toward DA sensing would not degrade over time. In addition, the electrode fabrication reproducibility was tested using three different NPC-2 modified GCEs in PBS solution for 10 mM DA at a scan rate of 100 mV s^{-1}. Each electrode exhibited similar electrochemical behavior peak current values, with a standard deviation of 1.05%. Moreover, the electrochemical storage stability of the NPC-2 modified GCE was examined after repetitive usage over days, 4 days/week and 2 weeks. The NPC-2 modified GCE kept under room temperature in PBS solution maintained 86% of its original current, with a standard deviation of 1.5% over 2 weeks. Conclusively, from the reproducibility and stability results, the NPC-2 modified GCE is a promising sensor for the detection of DA [10,40–44].

The enhanced electrochemical behavior of NPC-GCE toward DA detection originates from the remarkable properties of NPC. The large number of graphitic sites with few defects on NPC induced a high electrocatalytic activity toward DA with very low oxidation potential and high peak current. Moreover, owing to the strong interaction between C–N and the unique electronic structure, NPC facilitates fast electron transfer during the electrochemical reaction. Finally, the high surface area and foam-like porous network of NPC act like nano-tunnels to facilitate fast mass transfer at the electrode-electrolyte interface, which is the reason for the ultrahigh sensitivity of the electrode. The results indicate that NPC materials prepared through cost-effective and straightforward techniques by utilizing sustainable biomass energy resources are more efficient than previously reported materials. Therefore, the exclusive built-in properties of the AHS biomass precursor stands as a promising benchmark for achieving desirable electrode materials for the detection of neurotransmitters with ultrahigh sensitivity.

3.4. Computational studies

The DFT calculations were performed to answer the following questions: (i) Does the nitrogen doping enhance the interaction between DA and the NPC material? (ii) Does the NPC material sense DA more than UA? (iii) What type of interaction is present between the NPC material and the biomolecules? To model the NPC sheets, a basic amorphous carbon structure was taken from the work of Deringer et al. [47]. The nitrogen atoms were doped on the amorphous carbon surface by replacing several atoms from the 4-membered to the 9-membered carbon rings to form C–N bonds while the oxygen atoms were doped

Table 5
Experimental and theoretical elemental composition (%) of the modeled NPC sheets.

Atom Symbol	No. of atoms (Modeled AC)		Elemental composition (%)		
			Experimental	Theoretical	
	NPC(N)	NPC(O)	NPC-2	NPC(N)	NPC(O)
	146	145	85.14	85	86
N	10	2	6.18	6	1
O	16	22	8.68	9	13

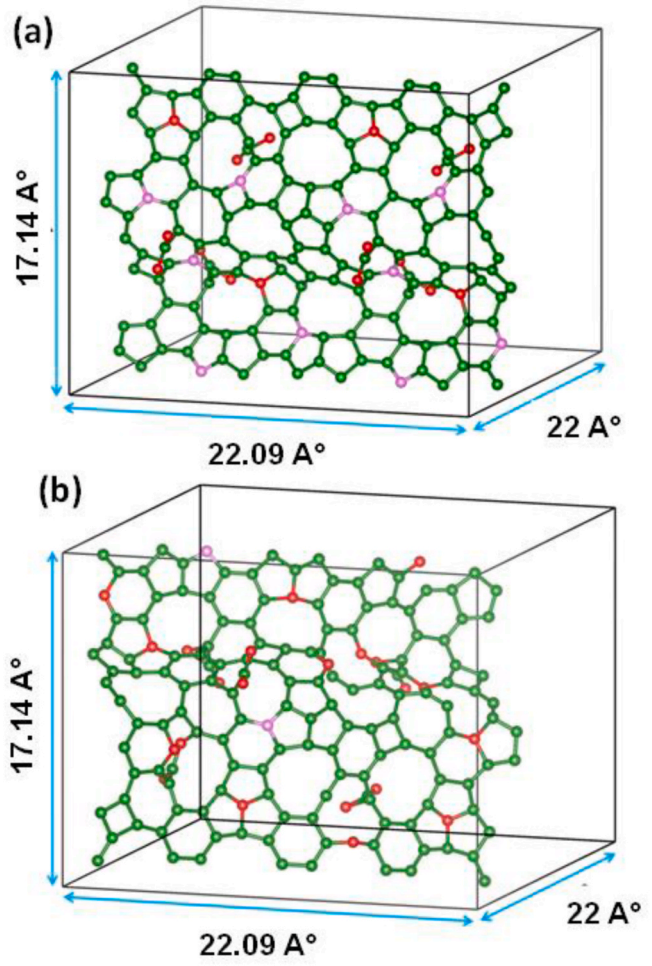

Fig. 8. DFT geometry optimized unit cell along with the top and side views of (a) nitrogen-rich and (b) oxygen-rich porous carbon sheets.

at the surface to form C–O–C bonds, along with the addition of an O–C=O group, which protruded from the surface of the amorphous carbon. The experimentally synthesized NPC materials showed three different elemental compositions of carbon, nitrogen, and oxygen. The percentage of atom compositions in Table 1 reveals that NPC-2 is rich in nitrogen atoms, whereas the NPC-1 and NPC-3 materials are oxygen-rich. Accordingly, we modeled two different NPC sheets, one where the nitrogen-rich sheet, NPC(N), resembles the NPC-2 material and the other where the oxygen-rich sheet, NPC(O), is composed of 86% carbon, 1% nitrogen, and 13% oxygen. The elemental compositions of the modeled NPC sheets are given in Table 5.

The lattice dimensions of the NPC sheets along the *x* and *y* directions were found to be 17.14 Å × 22.09 Å, respectively. The width along the protrusion of the functional groups was about 7.92 Å, and a vacuum layer of 22 Å was provided along the *z*-direction in order to reduce the artificial interactions due to periodic boundary conditions imposed on the simulations. The structurally minimized NPC sheets consisted of oxygen and nitrogen doping on the surface of the porous carbon sheet, along with O–C=O functional groups protruding from the carbon sheet along both the top and bottom, as shown in Fig. 8a and b, respectively. The top and side views of the NPC(N) and NPC(O) sheets are given in Figs. S4 and S5, respectively. The energy minimized sheets were considered for the interaction with biomolecules. The DA and UA molecules were structurally minimized with the same supercell configuration as that of the NPC sheet, and the minimum energy configurations were considered for further interaction studies.

3.4.1. Interaction of NPC(N) and NPC(O) sheets with dopamine molecule

To understand the effect of nitrogen doping on the interaction between DA and the NPC materials, the DA was placed in all possible orientations over the NPC(N) and NPC(O) sheets. Several orientations of DA were considered for the interaction, and the minimum energy corresponded to the perpendicular position on the NPC(N) and NPC (O) sheets, as shown in Fig. 9a and b, respectively. Accordingly, the adsorption energy was stronger for the case where the $–NH_2$ group of DA was interlocked between two O–C=O groups of both the NPC(N) and NPC(O) sheets. However, the adsorption energy between the NPC materials and the DA molecule (Table 6) showed a stronger interaction of DA with the NPC(N) sheet than with the NPC(O) sheet in both the gas and aqueous phase. Furthermore, the interaction of DA with the NPC materials was more highly stabilized in the aqueous phase than in the gas phase, which led to higher adsorption energy in the presence of a solvent. It is worth mentioning that in spite of the interaction site remaining the same in both NPC materials, the nitrogen-rich porous carbon sheet showed an increase in the adsorption energy of about 0.13 eV and 0.41 eV in the gas and aqueous phase, respectively, as compared to the oxygen-rich porous carbon sheet. Correspondingly, the stronger interaction was due to the presence of highly electronegative nitrogen atoms near the carbon atoms, which created localized negative charges over the sheet. The role of nitrogen in enhancing the interaction between the sheet and the molecule is substantiated in the next section.

3.4.2. Interaction of NPC(N) sheet with DA and UA molecules

Once the role of nitrogen atoms in enhancing the interaction with DA was validated, we then analyzed the interaction of the NPC(N) sheet with the DA/UA biomolecules. As discussed earlier, the minimum energy configuration of NPC(N) with DA corresponds to the interaction of the $–NH_2$ group of DA with the two O–C=O groups of the NPC(N) sheet. However, in the case of UA, out of various configurations, the minimum energy configuration was obtained for the parallel orientation of UA over the NPC(N) sheet (Fig. 10). The adsorption energies of the NPC(N) sheet with DA and UA in both gas and solvent phases are shown in Table 6. The adsorption of DA is stronger by 0.03 eV in gas and by 0.12 eV in the aqueous phase when compared to UA. This shows that the NPC (N) sheet was more selective toward DA than toward UA, which correlated well with the experimental results. Furthermore, to probe the nature of the interaction between the NPC(N) sheet and the DA/UA biomolecules, an Atoms in Molecules (AIM) analysis was performed using AIM-UC software, and the corresponding electron densities and their Laplacians are shown in Table 7.

AIM analysis [48] is widely used to describe the nature and strength of bonds using topological parameters such as the electron density (ρ) and its Laplacian ($\nabla^2\rho$) at the bond critical point (BCP) [49]. A BCP where the gradient of the electron density is zero between each pair of nuclei, denoted as the (3, −1) critical point, represents the formation of a chemical bond. A negative value of its Laplacian ($\nabla^2\rho$) implies the covalent character of the bond, whereas a positive $\nabla^2\rho$ shows non-covalent interactions such as ionic, van der Waals, and hydrogen bonding. Specifically, in the present work, the electron density (ρ) ranged from 0.0012 a. u. to 0.0033 a. u., whereas the Laplacian ($\nabla^2\rho$) ranged from 0.0054 a. u. to 0.0125 a. u. This shows the presence of

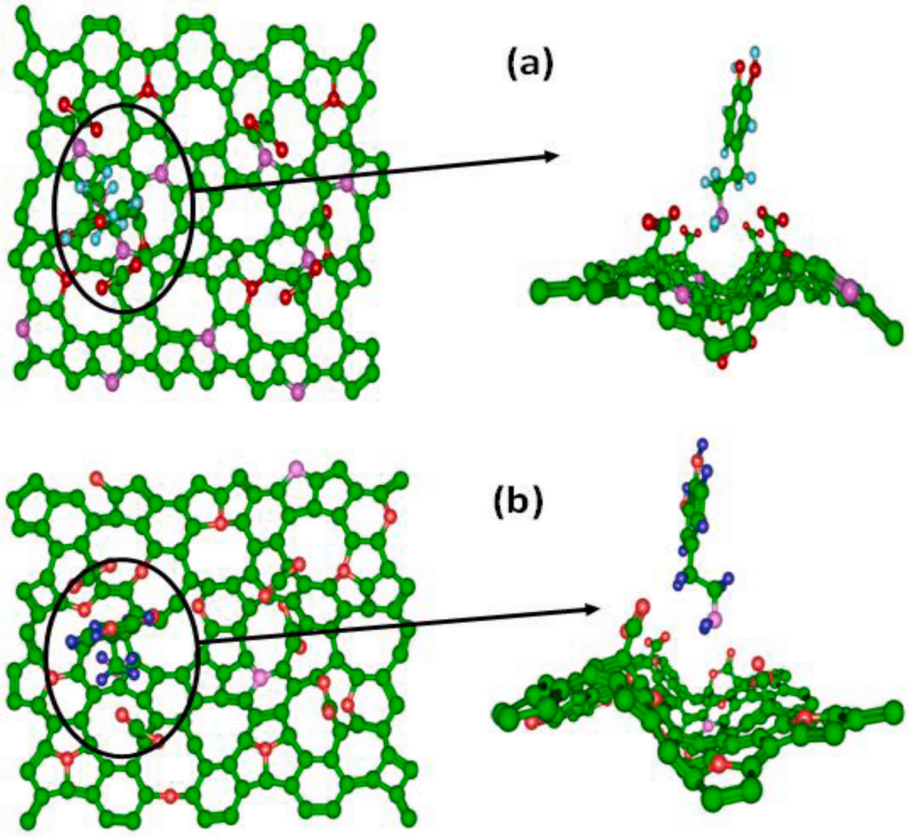

Fig. 9. Optimized geometry of (a) nitrogen-rich and (b) oxygen-rich porous carbon sheets with DA.

Table 6
Adsorption energy (eV) of NPC sheets with DA and uric acid.

Adsorption energy, E_{ads} (eV)		
Complex	Gas phase	Solvent (water) phase
NPC(N) with DA	−0.21	−0.64
NPC(O) with DA	−0.08	−0.23
NPC(N) with uric acid	−0.18	−0.52

hydrogen bonds, which are characterized by ρ values on the order ~10^{-2} a. u., with a lower and positive $\nabla^2\rho$, as proposed by Popelier et al. [50,51]. The BCPs for NPC(N) with DA (Table 7 and Supplementary Fig. S6) show the presence of two C–H···O bonds and one N–H···O bond. The two C–H···O bonds, with bond lengths of 2.31 Å and 2.62 Å, respectively, show ρ values of 0.0033 a. u. and 0.0018 a. u., respectively, with corresponding $\nabla^2\rho$ values of 0.0125 a. u. and 0.0090 a. u., respectively. The N–H···O bond is characterized by a bond length of 2.67 Å, with a ρ of 0.0023 a. u. and a $\nabla^2\rho$ of 0.0102 a. u. However, the interaction between NPC(N) and UA (Fig. S7) stems from the formation of one N–H···O bond with a bond length of 2.66 Å (ρ = 0.0012 a. u. and $\nabla^2\rho$ = 0.0054 a. u.). Conclusively, from the AIM analysis, we infer that the interaction between NPC(N) and the biomolecules are due to the presence of weaker hydrogen bonds. Additionally, dopamine forms more hydrogen bonds with the NPC(N) sheet than UA, which accounts for the stronger adsorption of DA to the NPC(N) sheet.

To understand the charge transfer between the NPC(N) surface and a biomolecule, the charge density difference plot (CDDP) was obtained, as shown in Fig. 11a and b. The CDDP validates the AIM results, showing that in the case of the DA molecule, the charges are transferred from the –NH_2 group to the O–C=O group of the NPC(N) sheet. Simultaneously, there is a charge transfer from the NPC(N) sheet to the nitrogen atom of the DA molecule. In addition to this, the O–C=O group of the NPC(N)

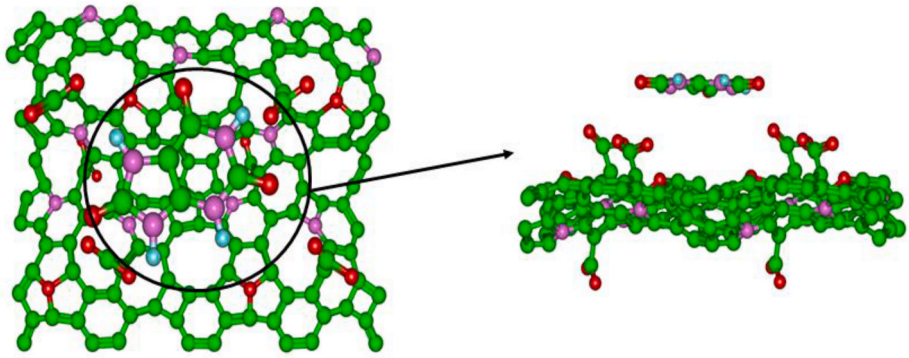

Fig. 10. Optimized geometry of nitrogen-rich porous carbon [NPC (N)]sheet with uric acid.

Table 7
Bond length, electron density, and Laplacian of electron density values of hydrogen bonds in biomolecules (DA/UA) interacted NPC (N) sheets.

Complex	Bond type	$R_{(H\cdots O)}$ (Å)	ρ (a.u.)	$\nabla^2\rho$ (a.u.)
NPC(N)/DA	C_{147}-$H_1\cdots O_{11}$	2.31	0.0033	0.0125
	C_{149}-$H_3\cdots O_{16}$	2.62	0.0018	0.0090
	N_{11}-$H_8\cdots O_{16}$	2.67	0.0023	0.0102
NPC(N)/UA	N_{14}-$H_4\cdots O_{11}$	2.66	0.0012	0.0054

sheet accepts an electron from the –CH bond of the DA molecule, whereas, in the case of uric acid, the molecule is stabilized owing to a charge transfer between the edge oxygen atoms of the UA molecule and the O–C=O group of the NPC sheet. Table 8 shows the quantitative values of charges transferred between the NPC sheet and the biomolecules (DA and UA). In the case of the DA interaction, the H atom loses average charges of |0.026|e and |4.5E-5|e via the C–H···O bonds and N–H···O bonds, respectively. Subsequently, the sheet gains an average of |0.0041|e charges. However, in the case of the UA interaction over the NPC(N) sheet, the molecule loses |4.3E-5|, whereas the sheet gains |0.0013|e via the N–H···O bond. Accordingly, it is evident from the charge-transfer plot and the charge differences that the charges are transferred from the biomolecules to the NPC sheet. In addition to this, a higher amount of charge transfer is due to the interlocking of DA molecules to the NPC sheet, which leads to the higher adsorption energy of DA as compared to UA.

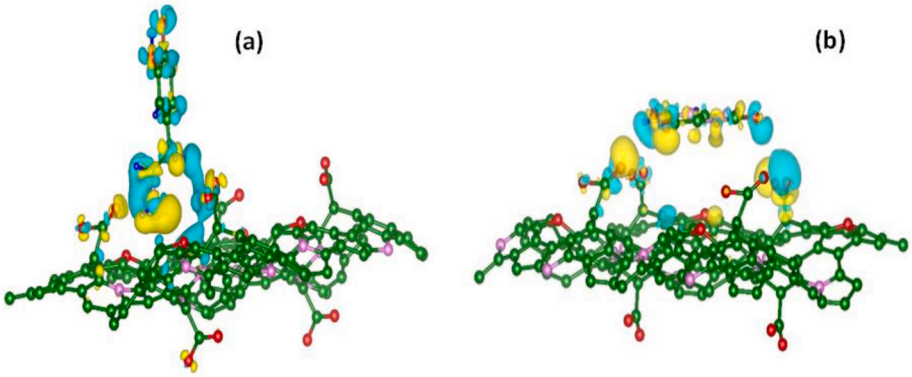

Fig. 11. (a and b) Charge density difference plot of nitrogen-rich porous carbon sheet with (a) dopamine and (b) uric acid. Yellow region represents charge accumulation, whereas cyan region represents charge depletion. (For interpretation of the references to colour in this figure legend, the reader is referred to the Web version of this article.)

Table 8
Difference in charge (Δq in e) between the nitrogen-rich porous carbon sheet and biomolecules (dopamine and uric acid).

Complex	Bond type	Charge (q in e)					
		Biomolecule			NPC(N) sheet		
		$q^{Before}_{interaction}$	$q^{After}_{interaction}$	|Δq|	$q^{Before}_{interaction}$	$q^{After}_{interaction}$	|Δq|
NPC(N)/DA	C_{147}-$H_1\cdots O_{11}$	1.0172	0.9919	0.0253	7.9550	7.9590	0.0040
	C_{149}-$H_3\cdots O_{16}$	1.0198	0.9928	0.0271	7.9609	7.9652	0.0043
	N_{11}-$H_8\cdots O_{16}$	4.5E-5	0	4.5E-5			
NPC(N)/UA	N_{14}-$H_4\cdots O_{11}$	2E-5	−2.3E-5	4.3E-5	7.9564	7.9577	0.0013

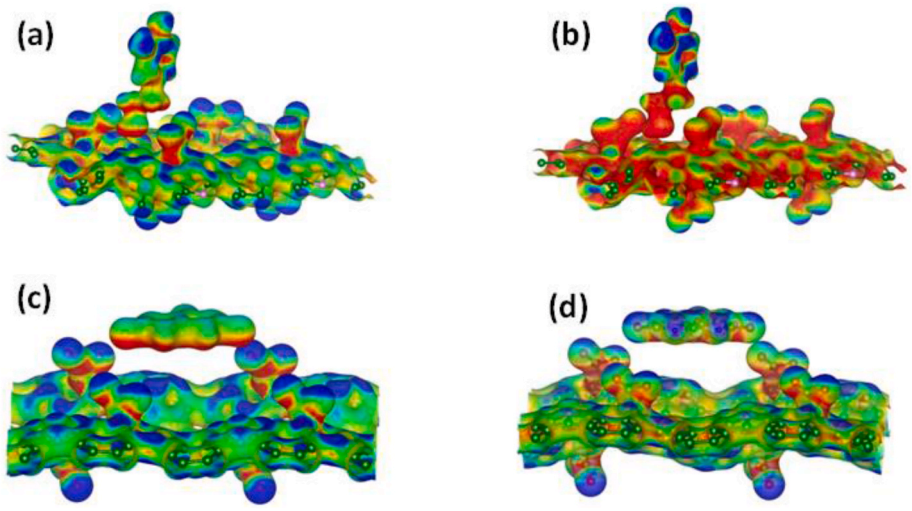

Fig. 12. Fukui function plots of nitrogen-rich and porous carbon sheets with (a,b) dopamine and (c, d) uric acid. (a, c) Electrophilic (f^-) attack and (b, d) nucleophilic (f^+) attack.

A Fukui function plot is a useful tool for understanding the redox sites of a system under study [52]. The blue region is highly reactive, whereas the red region is the least reactive. The Fukui function plots shown in Fig. 12reveal that the entire NPC(N) sheet is highly electrophilic owing to the disordered carbon layer, in addition to the presence of oxygen and nitrogen atoms. In particular, the redox sites of NPC(N) with DA can be identified from Fig. 12a and b, which show that the O–C=O group of NPC(N) is the acceptor site, which is highly electrophilic, whereas the tail of DA (both the –CH and $–NH_2$ group) is the donor site. However, in the case of UA (Fig. 12c and d), the O–C=O group of NPC(N) is the acceptor site, and the edge oxygen atoms act as donor sites. Therefore, charge transfer occurs via the biomolecules to the NPC(N) sheet, which is in agreement with the charge difference plots and values, as discussed above.

4. Conclusion

Foam-like porous activated carbon materials were successfully sequestered from *Artocarpus heterophyllus* seed starch through a single-step KOH activation route. As a result of activation at 700 °C/N_2, the activated carbon material had a large surface area (756 $m^2\ g^{-1}$), sufficient porosity (0.59 $cm^3\ g^{-1}$), and an exceptional amount of nitrogen functionalities (6.8 at. wt%). These exceptional features benefited the activated carbon material when it was used as an electrode material for DA electrochemical detection. The large surface area and porosity of the carbon surface enabled higher ionic conductivity and migration of ionic species. The inherited nitrogen atoms were anchored to the available active sites of carbon and provided wettability for DA molecule adsorption. Thus, fast electron transport in the circuit offered a superior increase in the current (13.95 μA) during the determination of DA at a very low onset potential (80 mV). In summary, the effective features of nitrogen-inherited carbon sensed DA across a wide linear range (30–90 μM and 200–400 μM), with a low LOD (2.74 nM) and superior sensitivity (4.64 μA $\mu M^{-1}\ cm^{-2}$). Hence, the nitrogen-inherited activated carbon sensor derived from AHS activation at 700 °C is reproducible, reusable, feasible, and biocompatible toward DA detection. The theoretical results revealed that the interaction of the dopamine molecule with the NPC sheet was stronger than that with the oxygen-rich porous carbon sheet. Subsequently, the dopamine molecule showed a stronger interaction with the NPC sheet than the UA molecule. The AIM analysis, charge transfer plot, charge difference value, and redox sites revealed the presence of weak hydrogen bonds, and the charges were transferred from the biomolecules to the NPC sheet. The stronger interaction of DA than UA corresponds to the presence of a greater number of hydrogen bonds owing to the interlocking of the DA molecule to the NPC sheet. Therefore an NPC sheet with a greater number of acceptor functional groups such as O–C=O can greatly enhance the electrochemical sensing ability.

Declaration of competing interest

The authors declare that they have no known competing financial interests or personal relationships that could have appeared to influence the work reported in this paper.

Acknowledgement

Dr A. Agnes Lincy would like to thank the Department of Science and Technology, India, for providing financial support [DST/INSPIRE Fellowship/2015/IF150672]. Prof. L. Senthil kumar would like to thank the University Grants Commission, New Delhi, India, for providing a fund to establish High-Performance Computing facility, under the Center with Potential for Excellence in Particular Area (CPEPA) scheme [Grant no.: 2-8/2016 (NS/PE) dated October 03, 2016]. Prof. Yun Sung Lee gratefully acknowledges the National Research Foundation of Korea (NRF) grant funded by the Korea government (Ministry of Science, ICT & Future Planning) (2019R1A4A2001527).

Appendix A. Supplementary data

Supplementary data to this article can be found online at https://doi.org/10.1016/j.matchemphys.2020.124094.

References

[1] B. Si, E. Song, Recent advances in the detection of neurotransmitters, Chemosensors 6 (2018) 1–24.
[2] W. Menegas, K. Akiti, R. Amo, N. Uchida, M. Watabe-Uchida, Dopamine neurons projecting to the posterior striatum reinforce avoidance of threatening stimuli, Nat. Neurosci. 21 (2018) 1421–1430.
[3] X. Dong, Z. Liao, D. Gritsch, Y. Hadzhiev, Y. Bai, J.J. Locascio, B. Guennewig, G. Liu, C. Blauwendraat, T. Wang, Enhancers active in dopamine neurons are a primary link between genetic variation and neuropsychiatric disease, Nat. Neurosci. 21 (2018) 1482–1492.
[4] N.D. Volkow, J.S. Fowler, S.J. Gatley, J. Logan, G.-J. Wang, Y.-S. Ding, S. Dewey, PET evaluation of the dopamine system of the human brain, J. Nucl. Med. 37 (1996) 1242–1255.
[5] A. Shrivastava, V.B. Gupta, Methods for the determination of limit of detection and limit of quantitation of the analytical methods, Chronicles Young Sci. 2 (2011) 21–25.
[6] A. Arroquia, I. Acosta, M. Pilar García Armada, Self-assembled gold decorated polydopamine nanospheres as electrochemical sensor for simultaneous determination of ascorbic acid, dopamine, uric acid and tryptophan, Mater. Sci. Eng. C 109 (2020), 110602.
[7] L. Durai, S. Badhulika, Facile synthesis of large area pebble-like β-$NaFeO_2$ perovskite for simultaneous sensing of dopamine, uric acid, xanthine and hypoxanthine in human blood, Mater. Sci. Eng. C 109 (2020), 110631.
[8] Y. Zhuang, X. Zhang, Q. Chen, S. Li, H. Cao, Y. Huang, Co_3O_4/CuO hollow nanocage hybrids with high oxidase-like activity for biosensing of dopamine, Mater. Sci. Eng. C 94 (2019) 858–866.
[9] J. Galindo-de-la-Rosa, L. Arriaga, A. Álvarez, N. Arjona, A. Déctor, A. Chavéz-Ramírez, V. Vallejo-Becerra, J. Ledesma-García, NiAl layered double hydroxides and PdNiO as multifunctional anodes for prospective self-powered lab-on-a-chip dopamine sensors, ChemNanoMat 4 (2018) 688–697.
[10] X. Liu, E. Shangguan, J. Li, S. Ning, L. Guo, Q. Li, A novel electrochemical sensor based on FeS anchored reduced graphene oxide nanosheets for simultaneous determination of dopamine and acetaminophen, Mater. Sci. Eng. C 70 (2017) 628–636.
[11] M. Wang, L. Zhong, M. Cui, W. Liu, X. Liu, Nanomolar level acetaminophen sensor based on novel polypyrrole hydrogel derived N-doped porous carbon, Electroanalysis 31 (2019) 711–717.
[12] X. Li, H. Li, T. Liu, Y. Hei, M. Hassan, S. Zhang, J. Lin, T. Wang, X. Bo, H.-L. Wang, The biomass of ground cherry husks derived carbon nanoplates for electrochemical sensing, Sensor. Actuator. B Chem. 255 (2018) 3248–3256.
[13] A. Savk, B. Özdil, B. Demirkan, M.S. Nas, M.H. Calimli, M.H. Alma, I. Abdullah, M. Asiri, F. Şen, Multiwalled carbon nanotube-based nanosensor for ultrasensitive detection of uric acid, dopamine, and ascorbic acid, Mater. Sci. Eng. C 99 (2019) 248–254.
[14] S. Meenakshi, S. Jancy Sophia, K. Pandian, High surface graphene nanoflakes as sensitive sensing platform for simultaneous electrochemical detection of metronidazole and chloramphenicol, Mater. Sci. Eng. C 90 (2018) 407–419.
[15] T. Aparna, R. Sivasubramanian, M.A. Dar, One-pot synthesis of Au-Cu_2O/rGO nanocomposite based electrochemical sensor for selective and simultaneous detection of dopamine and uric acid, J. Alloys Compd. 741 (2018) 1130–1141.
[16] M. Wang, H. Shi, M. Cui, W. Liu, X. Liu, Ultrasensitive electrochemical determination of Sunset Yellow in foods using size-tunable nitrogen-doped carbon spheres, J. Electrochem. Soc. 166 (2019) B13.
[17] W. Zhang, L. Liu, Y. Li, D. Wang, H. Ma, H. Ren, Y. Shi, Y. Han, B.-C. Ye, Electrochemical sensing platform based on the biomass-derived microporous carbons for simultaneous determination of ascorbic acid, dopamine, and uric acid, Biosens. Bioelectron. 121 (2018) 96–103.
[18] M. Wang, L. Bai, L. Zhang, G. Sun, X. Zhang, S. Dong, A microporous silk carbon–ionic liquid composite for the electrochemical sensing of dopamine, Analyst 141 (2016) 2447–2453.
[19] S.F. Rahman, K. Min, S.-H. Park, J.-H. Park, J.C. Yoo, D.-H. Park, Selective determination of dopamine with an amperometric biosensor using electrochemically pretreated and activated carbon/tyrosinase/Nafion®-modified glassy carbon electrode, Biotechnol. Bioproc. Eng. 21 (2016) 627–633.
[20] N. Jia, Z. Wang, G. Yang, H. Shen, L. Zhu, Electrochemical properties of ordered mesoporous carbon and its electroanalytical application for selective determination of dopamine, Electrochem. Commun. 9 (2007) 233–238.
[21] V. Veeramani, R. Madhu, S.-M. Chen, B.-S. Lou, J. Palanisamy, V.S. Vasantha, Biomass-derived functional porous carbons as novel electrode material for the practical detection of biomolecules in human serum and snail hemolymph, Sci. Rep. 5 (2015), 10141.
[22] A.S. Ahammad, N. Odhikari, S.S. Shah, M.M. Hasan, T. Islam, P.R. Pal, M.A. A. Qasem, M.A. Aziz, Porous tal palm carbon nanosheets: preparation, characterization and application for the simultaneous determination of dopamine and uric acid, Nanoscale Adv. 1 (2019) 613–626.

[23] H. Zhou, J. Chen, T. Huang, D. Chen, Y. Wu, F. Zheng, H. Yu, S. Li, Uniformly distributed and in situ iron–nitrogen co-doped porous carbon derived from pork liver for rapid and simultaneous detection of dopamine, uric acid, and paracetamol in human blood serum, New J. Chem. 41 (2017) 2081–2089.
[24] P. Rupa Kasturi, R. Kalai Selvan, Y.S. Lee, Pt decorated Artocarpus heterophyllus seed derived carbon as an anode catalyst for DMFC application, RSC Adv. 6 (2016) 62680–62694.
[25] P. Rupa Kasturi, A. Arunchander, D. Kalpana, R. Kalai Selvan, Bio-derived carbon as an efficient supporting electrocatalyst for the oxygen reduction reaction, J. Phys. Chem. Solid. 124 (2019) 305–311.
[26] P. Sennu, V. Aravindan, Y.-S. Lee, High energy asymmetric supercapacitor with 1D@ 2D structured $NiCo_2O_4$@ Co_3O_4 and jackfruit derived high surface area porous carbon, J. Power Sources 306 (2016) 248–257.
[27] S. Grimme, Semiempirical GGA-type density functional constructed with a long-range dispersion correction, J. Comput. Chem. 27 (2006) 1787–1799.
[28] J.P. Perdew, K. Burke, M. Ernzerhof, Generalized gradient approximation made simple, Phys. Rev. Lett. 77 (1996) 3865–3868.
[29] P.E. Blöchl, Projector augmented-wave method, Phys. Rev. B 50 (1994) 17953–17979.
[30] G. Kresse, D. Joubert, From ultrasoft pseudopotentials to the projector augmented-wave method, Phys. Rev. B 59 (1999) 1758–1775.
[31] G. Kresse, J. Furthmüller, Efficiency of ab-initio total energy calculations for metals and semiconductors using a plane-wave basis set, Comput. Mater. Sci. 6 (1996) 15–50.
[32] G. Kresse, J. Furthmüller, Efficient iterative schemes for ab initio total-energy calculations using a plane-wave basis set, Phys. Rev. B 54 (1996) 11169–11186.
[33] H.J. Monkhorst, J.D. Pack, Special points for Brillouin-zone integrations, Phys. Rev. B 13 (1976) 5188–5192.
[34] S. Grimme, J. Antony, S. Ehrlich, H. Krieg, A consistent and accurate ab initio parametrization of density functional dispersion correction (DFT-D) for the 94 elements H-Pu, J. Chem. Phys. 132 (15) (2010) 154104.
[35] S. Grimme, S. Ehrlich, L. Goerigk, Effect of the damping function in dispersion corrected density functional theory, J. Comput. Chem. 32 (2011) 1456–1465.
[36] K. Mathew, R. Sundararaman, K. Letchworth-Weaver, T.A. Arias, R.G. Hennig, Implicit solvation model for density-functional study of nanocrystal surfaces and reaction pathways, J. Chem. Phys. 140 (2014), 084106.
[37] C. Fu, D. Yi, C. Deng, X. Wang, W. Zhang, Y. Tang, F. Caruso, Y. Wang, A partially graphitic mesoporous carbon membrane with three-dimensionally networked nanotunnels for ultrasensitive electrochemical detection, Chem. Mater. 29 (2017) 5286–5293.
[38] W. Kang, H. Li, M. Ai, S. Wei, H. Gao, J. Liu, Y. Qian, Synthesis of nitrogen-doped carbon and application in highly selective and sensitive dopamine sensing, Mater. Lett. 116 (2014) 374–377.
[39] Z. Zhang, K.L. More, K. Sun, Z. Wu, W. Li, Preparation and characterization of PdFe nanoleaves as electrocatalysts for oxygen reduction reaction, Chem. Mater. 23 (2011) 1570–1577.
[40] A. Ramachandran, S. Panda, S.K. Yesodha, Physiological level and selective electrochemical sensing of dopamine by a solution processable graphene and its enhanced sensing property in general, Sensor. Actuator. B Chem. 256 (2018) 488–497.
[41] B. Wang, Y. Wang, Y. Peng, X. Wang, N. Wang, J. Wang, J. Zhao, Nitrogen-doped biomass-based hierarchical porous carbon with large mesoporous volume for application in energy storage, Chem. Eng. J. 348 (2018) 850–859.
[42] I. Izanzar, M. Dahbi, M. Kiso, S. Doubaji, S. Komaba, I. Saadoune, Hard carbons issued from date palm as efficient anode materials for sodium-ion batteries, Carbon 137 (2018) 165–173.
[43] X. Liu, H. Wang, Y. Cui, X. Xu, H. Zhang, G. Lu, J. Shi, W. Liu, S. Chen, X. Wang, High-energy sodium-ion capacitor assembled by hierarchical porous carbon electrodes derived from Enteromorpha, J. Mater. Sci. 53 (2018) 6763–6773.
[44] M. Sevilla, G.A. Ferrero, N. Diez, A.B. Fuertes, One-step synthesis of ultra-high surface area nanoporous carbons and their application for electrochemical energy storage, Carbon 131 (2018) 193–200.
[45] X. Li, H. Li, T. Liu, Y. Hei, M. Hassan, S. Zhang, J. Lin, T. Wang, X. Bo, H.-L. Wang, The biomass of ground cherry husks derived carbon nanoplates for electrochemical sensing, Sensor. Actuator. B Chem. 255 (2018) 3248–3256.
[46] P. Wiench, Z. González, R. Menéndez, B. Grzyb, G. Gryglewicz, Beneficial impact of oxygen on the electrochemical performance of dopamine sensors based on N-doped reduced graphene oxides, Sensor. Actuator. B Chem. 257 (2018) 143–153.
[47] V.L. Deringer, G. Csányi, D.M. Proserpio, Extracting crystal chemistry from amorphous carbon structures, ChemPhysChem 18 (2017) 873–877.
[48] W. Kutzelnigg, Von R.F.W. Bader, Atoms in Molecules. A Quantum Theory. (Reihe: International Series of Monographs on Chemistry, vol. 22, Clarendon Press, Oxford, 1990. XVIII, 438 S., ISBN 0-19-855168-1. Angewandte Chemie, 104 (10), (1992), 1423-1423.
[49] P. Popelier, P.L.A. Popelier, Atoms in Molecules: an Introduction, Prentice Hall, 2000.
[50] P.L.A. Popelier, R.F.W. Bader, The existence of an intramolecular C H O hydrogen bond in creatine and carbamoyl sarcosine, Chem. Phys. Lett. 189 (1992) 542–548.
[51] U. Koch, P.L.A. Popelier, Characterization of C-H-O hydrogen bonds on the basis of the charge density, J. Phys. Chem. 99 (1995) 9747–9754.
[52] G.K. Jayaprakash, B.E.K. Swamy, B.N. Chandrashekar, R. Flores-Moreno, Theoretical and cyclic voltammetric studies on electrocatalysis of benzethonium chloride at carbon paste electrode for detection of dopamine in presence of ascorbic acid, J. Mol. Liq. 240 (2017) 395–401.